# Broadband, high resolution, sensitive spectrometer using an integrated optical phased array in silicon nitride and Fourier imaging

Zuyang Liu, Nicolas Le Thomas, and Roel Baets, *Life Fellow, IEEE*

*Abstract*—We present a novel hybrid configuration of a spectrometer consisting of an integrated $Si_3N_4$ optical phased array and a free-space Fourier-space imaging system. It combines broadband and high resolution performance in a small on-chip footprint. We achieve 0.5 nm resolution in a spectral range from 750 nm to 850 nm using an on-chip footprint of $0.56 \times 0.22$ mm$^2$. As a proof of concept, we retrieve the optical spectrum of a single frequency titanium sapphire laser. Using an image sensor cooled down to -20°C, the low detection limit is validated by measuring the optical spectrum of the Raman background generated by a laser pump propagating in a $Si_3N_4$ waveguide.

*Index Terms*—integrated spectrometer, optical phased array, photonic integrated circuit, Fourier imaging

## I. INTRODUCTION

**O**ptical spectrometers are crucial in various scientific and industrial fields, including environmental monitoring, medical diagnostics, telecommunications, and chemical analysis. Conventional benchtop spectrometers are often bulky and limited to laboratory environments. With the development of integrated photonics, the miniaturization of spectrometers has led to a wide range of portable and robust solutions suitable for more applications outside the laboratory, including agricultural analysis and underwater studies [1], [2]. It can also enable lab-on-a-chip applications [3], [4], [5]. Based on their working principles, integrated spectrometers can be roughly divided into categories that utilize dispersion, narrowband filtering, Fourier transform, or numerical reconstruction [6]. The first category features dispersive optics that spatially separate different frequencies, including echelle gratings [7] and arrayed waveguide gratings (AWG) [8], [9]. The second type selectively transmits different spectral components to different detectors using narrowband filters such as ring resonators and Mach Zehnder interferometers (MZI) [10], [11], [12]. The third one is usually called Fourier transform spectroscopy (FTS), where the spectrum is obtained by converting interferometric information in the time or spatial domain to the corresponding frequency domain using a Fourier transform [13], [14], [15]. The last category employs a series of components with distinct spectral responses and reconstructs the spectrum from a combined signal [16], [17]. It relies on advanced computational algorithms, high computational power and sometimes machine learning.

The reduction in size, namely the integration, typically leads to compromises in signal intensity, resolution, and spectral range. Integrated spectrometers often need special engineering to meet the requirements of specific applications. To address the low signal intensity, it is common to use cooled detectors to improve the signal-to-noise ratio (SNR). However, cooled detectors integrated in close proximity with photonic integrated circuits (PICs) can cause liquid condensation on the chip and incompatibilities in sensor packaging. More importantly, it affects the properties of liquid analytes in contact with the chip surface, which is a common scenario in biosensing applications. For instance, waveguide-enhanced Raman spectroscopy (WERS) detects the Raman signal of analyte molecules in the evanescent field of dielectric waveguides [18]. WERS can identify and quantify analytes by their structural "fingerprint", with a prospect to replace conventional, bulky Raman microscopes that are commonly used in biological and pharmaceutical applications. Despite its great specificity, WERS produces a signal intensity below the detection limit of conventional integrated spectrometers. It requires a spectrometer with low detection limit, broad spectral range, high resolution, and compatibility with liquid analytes.

In this manuscript, we present a broadband spectrometer based on an optical phased array (OPA) on a silicon nitride ($Si_3N_4$) platform. The OPA splits the light from an input waveguide into an array of waveguides with ascending delay length, each of which is connected to a grating coupler for off-chip coupling. It serves as a dispersive component that diffracts each wavelength to a unique far-field direction defined by the phase delay in the array of waveguides and the dispersion properties of the grating couplers at the end of each waveguide. This structure was previously described by Van Acoleyen *et al.* as a beam steering component on a silicon-on-insulator (SOI) platform [19]. Here we upgrade it for spectral analysis by using a Fourier-space imaging technique. The emission directions are mapped to points in the back focal plane of a collecting lens and imaged with a camera cooled to -20°C. The optical spectrum is reconstructed from images recorded with the camera. This novel configuration of a hybrid guided wave and free-space optical system offers comparable resolution with FTS and AWG with a much smaller footprint, as listed in table I. It also combines the convenient advantage of off-the-shelf, cooled image sensors. As the cooled component is spatially separated from the PIC

Zuyang Liu was with the Photonics Research Group, Department of Information Technology, Ghent University - IMEC when the work was conducted. She is now with the University of Toronto, Canada (zuyang.liu@utoronto.ca). Nicolas Le Thomas and Roel Baets are with the Photonics Research Group, Department of Information Technology, Ghent University - IMEC, 9052 Ghent, Belgium.

TABLE I
COMPARISON OF COMPACT DESIGNS OF SPECTROMETERS

| Reference | Type | Platform | Resolution (nm) | Footprint (mm$^2$) |
|-----------|------|----------|-----------------|--------------------|
| [20] | AWG | Si$_3$N$_4$ | 0.75 | 1.15×1.25 |
| [21] | AWG | SOI | 0.4 | 0.65×1.06 |
| [22] | AWG | SOI | 1.22 | 0.5×0.45 |
| [23] | FTS | LiNbO$_3$ | 5.5 | 10 |
| [24] | FTS | SOI | 0.2 | 0.6×2.5 |
| [25] | FTS | SOI | 3 | 1 |
| This work | OPA | Si$_3$N$_4$ | 0.5 | 0.56×0.22 |

where the sensing waveguide resides, such an approach is well-suited for biomedical applications with liquid analytes. In the following sections, we first discuss the working principle of the proposed spectrometer, followed by proof-of-concept demonstrations by measuring the spectra of a laser and of Raman signals.

## II. WORKING PRINCIPLE

The spectrometer consists of an integrated OPA and a Fourier imaging system in free space. As sketched in Fig. 1, the integrated OPA includes an input waveguide, a star coupler, an array of waveguides with increasing lengths, and an array of grating couplers connected to the waveguides. Light from the input waveguide is split into the waveguide array by the star coupler and emitted off-chip by the grating couplers. The emission direction can be characterized by two separate angles relative to the $z$-axis ($\theta_x$ and $\theta_y$) in $xz$- and $yz$-plane, respectively, as shown in the cross-sections of Fig. 1. The angle $\theta_x$ is determined by the diffraction condition of the grating couplers, while the emission angle $\theta_y$ is related to the phase delay between each emitter. Both angles change with the input wavelength, and each wavelength corresponds to a unique direction of ($\theta_x$, $\theta_y$). The unknown input wavelength can be determined from the emission direction. We use a Fourier imaging system (Fig. 2) to measure the emission direction of the quasi-parallel beam. Light emitted from the chip is first focused onto a point on the back focal plane of a microscope objective (MO). Then, the back focal plane is imaged onto a camera by a two-lens system with suitable magnification. The emission angle governs the lateral displacement of the light spot from the optical center. $\theta_x$ and $\theta_y$ correspond to displacements in two orthogonal directions on the camera captured images.

The diffraction angle $\theta_x$ relative to the $z$-axis is determined by the grating pitch $\Lambda$, effective index of grating $n_{gr}$, and wavelength $\lambda$ as

$$\sin\theta_x = \frac{n_{gr} - \lambda/\Lambda}{n_{clad}} \quad (1)$$

where $n_{clad}$ is the refractive index of the background material, which is air in our design ($n_{clad} = 1$). The angular dispersion in $x$-direction is thus given by

$$\frac{\mathrm{d}\sin\theta_x}{\mathrm{d}\lambda} = \frac{\mathrm{d}n_{gr}}{\mathrm{d}\lambda} - \frac{1}{\Lambda}. \quad (2)$$

We numerically estimate the effective index of a silica-cladded Si$_3$N$_4$ grating with 800 nm width, 300 nm total thickness, 200 nm etch depth, 500 nm pitch, and a fill factor of 0.5.
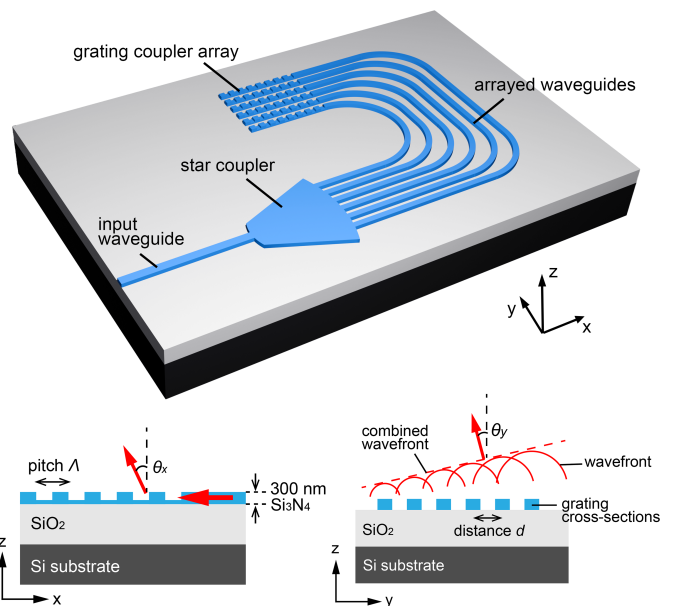


Fig. 1. Schematic of the integrated OPA. Light from the input waveguide is split into an array of waveguides with increasing lengths by a star coupler and then emitted out of the $xy$-plane by an array of grating couplers. The two bottom figures show the cross-sections of the gratings in $xz$- and $yz$-plane, respectively.
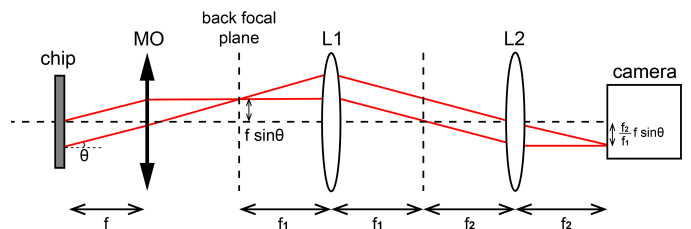


Fig. 2. Schematic of the Fourier imaging system, consisting of the chip, a microscope objective (MO), two lenses, and a camera. Parallel beam with an angle of direction $\theta$ is focused onto a point on the camera with a lateral displacement from the optical axis.

Around a wavelength of 850 nm, $\mathrm{d}n_{gr}/\mathrm{d}\lambda$ is found to be $-0.286/\mu$m. The angular dispersion is then calculated to be $-2.286/\mu$m, corresponding to $\mathrm{d}\theta_x/\mathrm{d}\lambda = -0.13°$/nm at 850 nm wavelength.

The emission angle $\theta_y$ is determined by the phase delay in the arrayed waveguides. The waveguides have a length difference of $\Delta L$ between adjacent ones, resulting in a phase difference of

$$\Delta\varphi = \frac{2\pi}{\lambda} n_{eff}\Delta L \quad (3)$$

where $n_{eff}$ is the effective index of the waveguide in the array. Light emitted from the array of grating couplers form a combined wavefront that is a quasi-plane wave. As depicted in the $yz$-cross-section in Fig. 1, the propagation direction $\theta_y$ of the combined wavefront is closely related to $\Delta\varphi$ as

$$\Delta\varphi = \frac{2\pi d}{\lambda} \sin\theta_y + m \cdot 2\pi \quad (4)$$

where $d$ is the center-to-center distance between grating couplers, and $m$ an integer representing the delayed order of the

phased array [26]. Combining eq. (3) and (4), $\theta_y$ is given by

$$\sin \theta_y = \frac{n_{eff}\Delta L}{d} - m\frac{\lambda}{d}. \tag{5}$$

And the angular dispersion in $y$-direction is

$$\frac{d\theta_y}{d\lambda} \approx \frac{d\sin\theta_y}{d\lambda} = \frac{dn_{eff}}{d\lambda}\frac{\Delta L}{d} - \frac{m}{d} \tag{6}$$

when angle $\theta_y$ is small. Around the wavelength of 850 nm, $dn_{neff}/d\lambda$ is found to be $-0.354/\mu$m. The angular full width half maximum (FWHM) of the beam width in radians is approximately

$$\Delta\theta_y \approx 0.886\frac{\lambda}{Nd\cos\theta_y} \tag{7}$$

where $N$ is the number of grating couplers in the array. When the angle $\theta_y$ is small, the FWHM can be further approximated to

$$\Delta\theta_y \approx 0.886\frac{\lambda}{Nd}. \tag{8}$$

Therefore, the spectral resolution $R$ in $y$-direction (i.e. the FWHM in wavelengths) can be estimated from eq. (6) and (8) as

$$R = \frac{\Delta\theta_y}{|d\theta_y/d\lambda|} = \frac{0.886\lambda}{N|\frac{dn_{eff}}{d\lambda}\Delta L - m|}. \tag{9}$$

Depending on the target application, different resolutions can be achieved by tuning the properties of the OPA. For the purpose of on-chip Raman spectroscopy, we aim to achieve a spectral resolution of below 1 nm, which is below the FWHM of the prominent Raman peaks of many liquid or solid substances. With 800-nm-wide and 300-nm-thick $Si_3N_4$ waveguides, we find a combination of $d = 1.6$ $\mu$m, $\Delta L = 25$ $\mu$m, $m = 27$, and $N = 32$ that gives a spectral resolution of around 0.6 nm around the wavelength of 850 nm. The angular dispersion in the $y$-direction is about -1.4°/nm, much faster than that in the $x$-direction. This is calculated for the fundamental TE mode in the strip waveguide.

Fig. 3 shows images of different wavelengths captured by the camera. The slow steering along the $x$-axis is due to the grating diffraction while the fast steering along the $y$-axis is because of the phased array. The field of view (FoV) is mainly determined by the numerical aperture (NA) of the microscope objective. It is designed in such a way that only one order of the phased array is captured. When the wavelength is increased from 800 nm to 802 nm, the previous order exits the FoV from the top and the next delayed order enters from the bottom. Moreover, light spots of different wavelengths from different orders of the phased array may share the same $y$-coordinate, imposing potential limitations on the spectral range of the proposed spectrometer. This is circumvented by the slower steering in the $x$-direction, which sufficiently separates different wavelengths from different orders horizontally. Therefore, the spectral range of the spectrometer is only primarily limited by the NA of the Fourier imaging system and transmission spectrum of the grating couplers. We estimate that it can easily cover over 200 nm spectral range with the aforementioned grating couplers and a MO with 0.28 NA.

In this work, we set the target spectral range to $750 - 870$ nm, which covers the Raman shift up to 1200 cm$^{-1}$
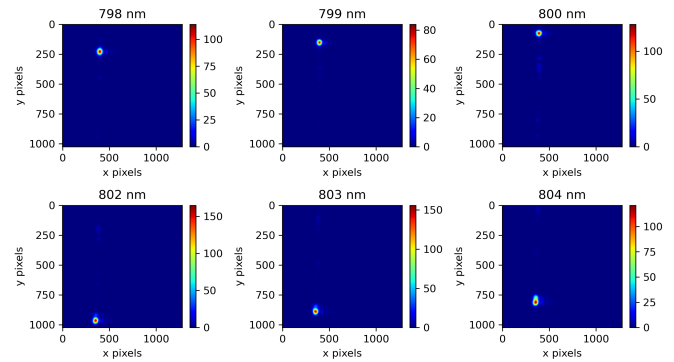


Fig. 3. Images in the Fourier space of the far-field emission diagram diffracted by the grating couplers of the OPA for different laser wavelengths. Pseudo-colored to show intensity.

with a conventional pump wavelength of 785 nm. This is sufficient to identify structurally simple analytes, such as isopropanol, ethanol, and dimethyl sulfoxide (DMSO). We use Lumerical MODE Solutions to estimate the effective indices of $Si_3N_4$ gratings and waveguides. Also, a minimum bend radius is found at 50 $\mu$m to prevent excess loss. Then, using the determined geometric parameters, we generate the design with a star coupler using a modified version of IPKISS AWG Designer [27].

## III. SPECTRUM OF A LASER

We fabricated a series of OPAs on a 300 nm thick $Si_3N_4$ layer, spaced from a silicon wafer by a 3 $\mu$m thick $SiO_2$ buffer layer using electron beam lithography (EBL) and reactive ion etching (RIE). A layer of hydrogen silsesquioxane (HSQ) is then spun onto the sample and cured at 400°C to form a $SiO_2$-like top cladding [28]. Fig. 4 shows the top view of an OPA with 32 waveguides in the array. The OPA has a small footprint of about $0.56 \times 0.22$ mm$^2$. The waveguides are 800 nm wide and 300 nm thick. These relatively large dimensions provide strong confinement of the lowest order guided mode and therefore reduce its sensitivity to phase error induced by width and thickness variations. The waveguide is not strictly single mode but the excitation of higher order modes is assumed to be very weak. Light is coupled in through a 3 $\mu$m-wide edge coupler, tapered down to the strip waveguide. Then it is tapered to 3 $\mu$m wide again to connect with a star coupler, where a slab mode is excited. An array of 32 waveguides is placed on an arc to collect light from the star coupler. The bend radius is 50 $\mu$m. The delay length difference $\Delta L$ is 24.9 $\mu$m. The center-to-center distance between gratings is 1.6 $\mu$m.

In this section, we present the methodology and results of measuring a test signal on the setup sketched in Fig. 5. We combine the output of a tunable laser and a supercontinuum light source through a 50:50 fiber splitter. This is to mimic the profile of a Raman signal with a broad waveguide background and a distinct analyte signal. The beam leaving the fiber is collimated in free space through a collimator. A half-wave plate and a polarizing beam splitter (PBS) ensure that the beam is linearly polarized and will only excite TE-modes in the PIC. Then the beam is split through a 50:50 beam splitter, coupling
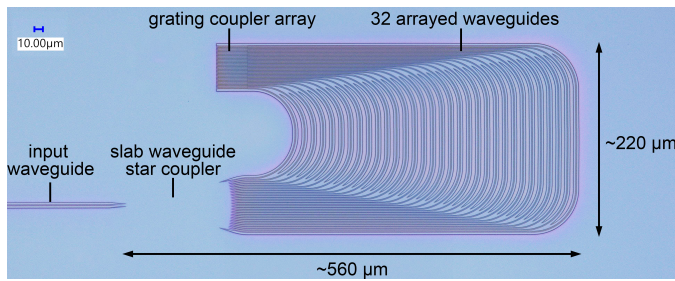
Fig. 4. Microscope image of the OPA fabricated on a $Si_3N_4$ platform using electron beam lithography. Waveguides are defined by etching 3 $\mu$m-wide trenches beside them.
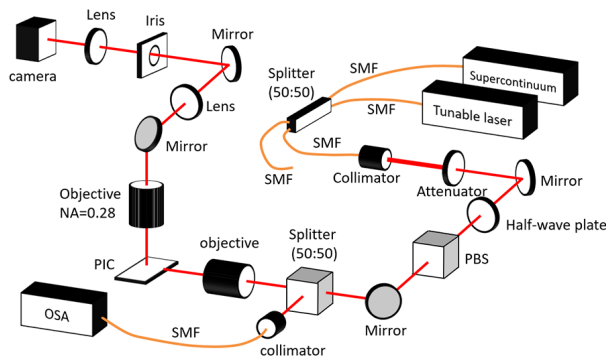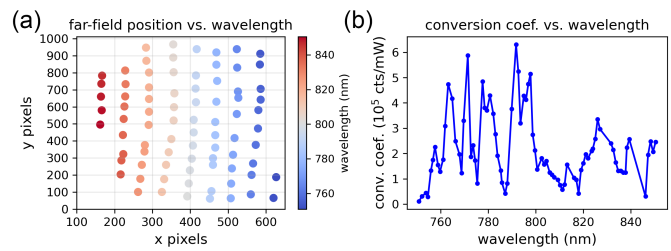


Fig. 6. (a) Light spot center in x- and y-axis of different wavelengths. (b) Conversion coefficient of the OPA spectrometer of different wavelength.



Fig. 5. Schematics of the experiment setup for the characterization of OPA spectrometers.
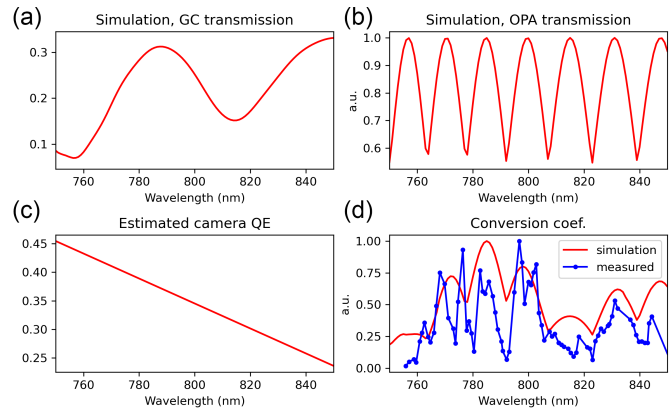


Fig. 7. Simulated transmission of (a) the grating couplers and (b) the optical phased array. (c) Quantum efficiency of the camera. (d) Conversion coefficients from simulations in (a), (b) and (c) and measurement.

half to a commercial optical spectrum analyzer (OSA) as a reference, while the other half is coupled into the PIC via a microscope objective. Light emitted from the OPA is focused onto the back focal plane of another microscope objective ($10\times$, NA 0.28), which is then imaged onto a camera through a two-lens system. The camera (Thorlabs DCU224M) has a sensor size of $6.0\times4.8$ mm$^2$ with square pixels of 4.65 $\mu$m wide. The two lenses have focal lengths of 200 mm and 100 mm, respectively, resulting in a magnification of $\times0.5$ from the objective back focal plane to the camera.

The measurement starts from a calibration process that reveals the relation between input wavelength and light spot position and intensity on the camera. We first couple only the tunable laser into the waveguide and tune the wavelength from 750 nm to 850 nm with a step size of 1 nm. Pictures are captured for each wavelength, as shown in Fig. 3. The light spot center of all wavelengths is visualized in Fig. 6(a). All examined wavelengths are nicely separated and resolved.

Fig. 6(b) shows the signal intensity collected on the camera, represented by a quantity named conversion coefficient (counts/mW), defined as the total number of counts divided by the input power before the in-coupling objective. The total number of counts is calculated by integrating the camera readout within the FWHM of the light spot. We can use the conversion coefficients to convert signal intensities on different far-field positions to wavelength-dependent power before the system. It is affected by several components in the system. For instance, from the simulated transmission

of the grating couplers presented in Fig. 7(a), we observe two dips: one around 760 nm due to back reflection of the grating and one around 810 nm due to reflection from the top interface of the Si substrate. Moreover, Fig. 7(b) shows that the normalized intensity of the primary peak of the OPA also varies with wavelength. Considering the steering of a main order beam, its peak intensity varies with angle according to the far-field envelope determined by a single grating. Further steering moves the next delayed order of the phased array into the FoV, causing abrupt increases in intensity. In addition, the quantum efficiency of the camera decreases when the wavelength increases, as shown in Fig. 7(c). Combining the three factors, we numerically estimate the conversion coefficient as the red curve in Fig. 7(d). Taking into account all uncertainties in the system, the intensity variation agrees reasonably well with the experimentally measured conversion coefficient.

From the calibration, it is observed that the average angular dispersion along the y-axis is around 81 pixels/nm, while the average FWHM in that direction is around 44 pixels. Hence the average spectral resolution is around 0.5 nm, agreeing with the theoretical estimation for a 32-waveguide OPA. The spectral range in the measurement is determined by the tunable range of the laser. It can be greatly expanded by replacing the tunable laser and changing to a higher NA objective. However, it is worth noting that imaging a larger NA onto the same camera may reduce the spot size compared to the pixel size, impacting the image resolution. It can be mitigated by increasing the angular dispersion while maintaining the spot size, replacing
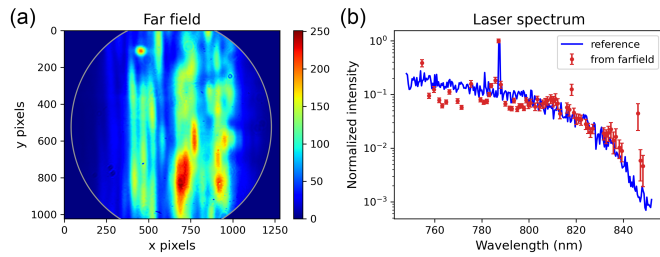
Fig. 8. (a) Far-field image of the test signal from a tunable laser and supercontinuum. The grey circle represents the exit pupil of the microscope objective. (b) Spectrum reconstructed from the far-field (red dots), along with reference spectrum obtained with the optical spectrum analyzer (blue curve).
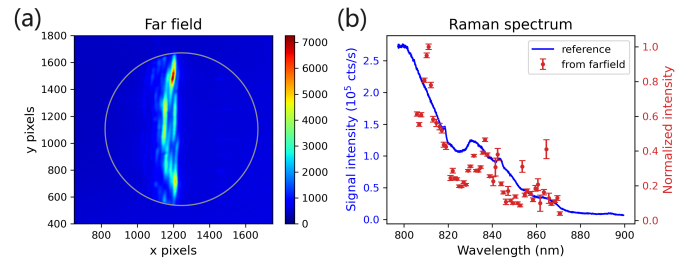


Fig. 9. (a) Far-field image of the Raman signal, ambient light removed, exposure time 300 s. The grey circle represents the exit pupil of the microscope objective. (b) Spectrum reconstructed from the far-field (red dots), along with reference spectrum obtained with the optical spectrum analyzer (blue curve).

the camera with a larger sensor area, or reducing the pixel size.

Then the test signal combining the tunable laser and the supercontinuum is coupled into the OPA. Fig. 8(a) shows the far-field image captured by the camera. The circular light spot on the top left corresponds to the distinct peak of the tunable laser. It is converted to a spectrum using positions and conversion coefficients acquired in the calibration process shown in Fig. 6. The result is shown in red dots in Fig. 8(b), where the error bar represents shot noise, background noise from ambient light, and readout noise of the camera. The noise is more prominent when the conversion coefficient is low. The outliers (e.g. around 850 nm) are due to low signal intensities and strong background noise. The same signal measured using a commercial optical spectrum analyzer (OSA) is included in Fig. 8(b) as reference. There is good agreement in the retrieved values of the wavelength and relative intensity.

## IV. SPECTRUM OF A RAMAN SIGNAL

The $Si_3N_4$ strip waveguide connecting the input edge coupler and the OPA is approximately 1 cm long. When a monochromatic pump is coupled into the waveguide, it generates a broadband background, being the so-called Raman background of the waveguide. It is intrinsic to the dielectric material forming the waveguide and imposes extra noise on the Raman signal of an analyte [29]. The intensity of the Raman background is comparable to Raman peaks of typical analytes. The diffracted far-field signal of the OPA in Fig. 9(a) allows us to retrieve the spectrum of the Raman background of a $Si_3N_4$ waveguide pumped by a 785 nm laser as plotted in Fig. 9(b) in red dots. The reference spectrum in Fig. 9(b) in blue curve corresponds to the Raman signal of the waveguide measured at the input of the waveguide in a reflection configuration using a 785 nm pump laser and a commercial spectrometer cooled down to -70°C. On top of the Raman background, a small peak around 843 nm (Raman shift 876 cm$^{-1}$) is induced by the HSQ cladding on top of the $Si_3N_4$ waveguide.

When using the OPA, the weak Raman signal generated by the strip waveguide is collected with a camera (QImaging Retiga LUMO) cooled down to -20°C. The CCD sensor size is 12.5×10 mm$^2$, roughly four times larger than the uncooled one used in the previous section. Therefore, to fully utilize the sensor area, we change the focal length of the last imaging lens from 100 mm to 200 mm to increase the magnification from

×0.5 to ×1 from the objective pupil to the camera. Also, a set of long-pass filters with a cutoff wavelength of 800 nm is added in front of the camera to remove the 785 nm pump, orders of magnitude stronger than the Raman signal.

The measurement starts from the same calibration process as presented in the previous section: sweep the input wavelength and record the far-field. The calibration wavelength range is 800 – 870 nm. To measure the Raman signal, we first couple the 785 nm pump laser and integrate the signal for 300 seconds. Then the pump laser is turned off to acquire an image of ambient light and dark counts, also with an exposure time of 300 seconds. Fig. 9(a) shows the far-field image of the Raman signal generated by the strip waveguide with the ambient and dark noise subtracted. Fig 9(b) shows that the spectrum converted from the far-field matches well the reference spectrum in wavelength and relative intensity. The outliers are once more due to low signal intensity and high background noise.

## V. CONCLUSION AND DISCUSSION

In this manuscript, we present a broadband spectrometer that has small on-chip footprint and high resolution. It consists of an integrated $Si_3N_4$ optical phased array (OPA) and a free-space Fourier imaging system. We present a proof-of-concept demonstration using an OPA with 32 waveguides fabricated on a $Si_3N_4$ platform with a footprint of 0.56×0.22 mm$^2$. A resolution of 0.5 nm is achieved in the spectral range extending from 750 nm to 870 nm. The wavelength range is expected in principle to reach several hundreds of nanometers as it is currently limited by the tunable range of the laser for the calibration. Measurement of a test laser signal shows good agreement in wavelength and relative intensity. We also measured a rather weak signal (waveguide Raman background with little analyte) using an image sensor cooled down to -20°C.

Compared to other integrated spectrometers, the advantages of the OPA spectrometer include broad spectral range, high resolution with a small on-chip footprint, ease to use off-the-shelf, cooled image sensors, and convenience to integrate free-space, high-rejection-ratio pump filters into a Raman sensing system. It achieves comparable spectral resolution with FTS and AWG with a much smaller on-chip footprint. For biomedical and pharmaceutical applications where the analyte needs to be kept above a certain temperature, it is also more

convenient to keep the cooled detector spatially separated from the sensing waveguides.

## REFERENCES

[1] L. P. Schuler, J. S. Milne, J. M. Dell, and L. Faraone, "MEMS-based microspectrometer technologies for nir and mir wavelengths," *Journal of Physics D: Applied Physics*, vol. 42, p. 133001, 2009.

[2] R. A. Crocombe, "Portable spectroscopy," *Applied spectroscopy*, vol. 72, no. 12, pp. 1701–1751, 2018.

[3] Y.-T. Wu, C.-E. Yang, C.-H. Ko, Y.-N. Wang, C.-C. Liu, and L.-M. Fu, "Microfluidic detection platform with integrated micro-spectrometer system," *Chemical Engineering Journal*, vol. 393, p. 124700, 2020. [Online]. Available: https://www.sciencedirect.com/science/article/pii/S1385894720306914

[4] B. Hinkov, F. Pilat, L. Lux, P. L. Souza, M. David, A. Schwaighofer, D. Ristanic, B. Schwarz, H. Detz, A. M. Andrews, B. Lendl, and G. Strasser, "A mid-infrared lab-on-a-chip for dynamic reaction monitoring," *Nature Communications*, vol. 13, p. 4753, 2022.

[5] K. M. Yoo, K.-C. Fan, M. Hlaing, S. Jain, S. Ning, Y. An, and R. T. Chen, "Lab-on-a-chip optical biosensor platform: a micro-ring resonator integrated with a near-infrared Fourier transform spectrometer," *Opt. Lett.*, vol. 48, no. 20, pp. 5371–5374, Oct 2023. [Online]. Available: https://opg.optica.org/ol/abstract.cfm?URI=ol-48-20-5371

[6] Z. Yang, T. Albrow-Owen, W. Cai, and T. Hasan, "Miniaturization of optical spectrometers," *Science*, vol. 371, no. 6528, p. eabe0722, 2021.

[7] S. Xie, Y. Meng, J. Bland-Hawthorn, S. Veilleux, and M. Dagenais, "Silicon nitride/silicon dioxide echelle grating spectrometer for operation near 1.55 $\mu$m," *IEEE Photonics Journal*, vol. 10, no. 6, pp. 1–7, 2018.

[8] P. Cheben, J. H. Schmid, A. Delage, A. Densmore, S. Janz, B. Lamontagne, J. Lapointe, E. Post, P. Waldron, and D. X. Xu, "A high-resolution silicon-on-insulator arrayed waveguide grating microspectrometer with sub-micrometer aperture waveguides," *Optics Express*, vol. 15, no. 5, pp. 2299–2306, 2007.

[9] A. van Wijk, C. R. Doerr, Z. Ali, M. Karabiyik, and B. I. Akca, "Compact ultrabroad-bandwidth cascaded arrayed waveguide gratings," *Optics Express*, vol. 28, no. 10, pp. 14 618–14 626, 2020.

[10] H. Xu and Y. Shi, "Flat-top CWDM (De)Multiplexer based on MZI with bent directional couplers," *IEEE Photonics Technology Letters*, vol. 30, no. 2, pp. 169–172, 2018.

[11] D. Munk, M. Katzman, Y. Kaganovskii, N. Inbar, A. Misra, M. Hen, M. Priel, M. Feldberg, M. Tkachev, A. Bergman, M. Vofsi, M. Rosenbluh, T. Schneider, and A. Zadok, "Eight-channel silicon-photonic wavelength division multiplexer with 17 GHz spacing," *IEEE Journal of Selected Topics in Quantum Electronics*, vol. 25, no. 5, pp. 1–10, 2019.

[12] C. Sun, Z. Chen, Y. Yin, Y. Ye, Y. Luo, H. Ma, J. Jian, Y. Shi, C. Zhong, D. Zhang, H. Lin, and L. Li, "Broadband and high-resolution integrated spectrometer based on a tunable FSR-free optical filter array," *ACS Photonics*, vol. 9, no. 9, pp. 2973–2980, 2022.

[13] E. Le Coarer, S. Blaize, P. Benech, I. Stefanon, A. Morand, G. Lérondel, G. Leblond, P. Kern, J. M. Fedeli, and P. Royer, "Wavelength-scale stationary-wave integrated Fourier-transform spectrometry," *Nature Photonics*, vol. 1, pp. 473–478, 2007.

[14] X. Nie, E. Ryckeboer, G. Roelkens, and R. Baets, "CMOS-compatible broadband co-propagative stationary Fourier transform spectrometer integrated on a silicon nitride photonics platform," *Optics Express*, vol. 25, no. 8, pp. A409–A418, 2017.

[15] H. Podmore, A. Scott, P. Cheben, A. V. Velasco, J. H. Schmid, M. Vachon, and R. Lee, "Demonstration of a compressive-sensing Fourier-transform on-chip spectrometer," *Optics Letters*, vol. 42, no. 7, pp. 1440–1443, 2017.

[16] B. Redding, S. F. Liew, R. Sarma, and H. Cao, "Compact spectrometer based on a disordered photonic chip," *Nature Photonics*, vol. 7, pp. 746–751, 2013.

[17] C. Yao, K. Xu, W. Zhang, M. Chen, Q. Cheng, and R. Penty, "Integrated recontructive spectrometer with programmable photonic circuits," *Nature Communications*, vol. 14, p. 6376, 2023.

[18] A. Dhakal, A. Z. Subramanian, P. Wuytens, F. Peyskens, N. Le Thomas, and R. Baets, "Evanescent excitation and collection of spontaneous Raman spectra using silicon nitride nanophotonic waveguides," *Optics Letters*, vol. 39, no. 13, pp. 4025–4028, 2014.

[19] K. Van Acoleyen, W. Bogaerts, and R. Baets, "Two-dimensional dispersive off-chip beam scanner fabricated on silicon-on-insulator," *IEEE Photonics Technology Letters*, vol. 23, no. 17, pp. 1270–1272, 2011.

[20] Z. Zhang, Y. Wang, and H. K. Tsang, "Tandem configuration of microrings and arrayed waveguide gratings for a high-resolution and broadband stationary optical spectrometer at 860 nm," *ACS Photonics*, vol. 8, no. 5, pp. 1251–1257, 2021.

[21] J. Zou, X. Ma, X. Xia, J. Hu, C. Wang, M. Zhang, T. Lang, and J.-J. He, "High resolution and ultra-compact on-chip spectrometer using bidirectional edge-input arrayed waveguide grating," *Journal of Lightwave Technology*, vol. 38, no. 16, pp. 4447–4453, 2020.

[22] C. Yang, Z. Zhu, X. Gao, Z. Xu, S. Han, Y. Chong, R. Min, Y. Yue, and Z. Duan, "Compact silicon-arrayed waveguide gratings with low nonuniformity," *Sensors*, 2024.

[23] D. Pohl, M. R. Escalé, M. Madi, F. Kaufmann, P. Brotzer, A. Sergeyev, B. Guldimann, P. Giaccari, E. Alberti, U. Meier, and R. Grange, "An integrated broadband spectrometer on thin-film lithium niobate," *Nature Photonics*, vol. 14, pp. 24–29, 2020.

[24] D. M. Kita, B. Miranda, D. Favela, D. Bono, J. Michon, H. Lin, T. Gu, and J. Hu, "High-performance and scalable on-chip digital fourier transform spectroscopy," *Nature Communications*, vol. 9, p. 4405, 2018.

[25] M. C. M. M. Souza, A. Grieco, N. C. Frateschi, and Y. Fainman, "Fourier transform spectrometer on silicon with thermo-optic non-linearity and dispersion correction," *Nature Communications*, vol. 9, p. 665, 2018.

[26] B. Bhandari, C. Wang, J.-Y. Gwon, J.-M. Heo, S.-Y. Ko, M.-C. Oh, and S.-S. Lee, "Dispersive silicon–nitride optical phased array incorporating arrayed waveguide delay lines for passive line beam scanning," *Scientific Reports*, vol. 12, p. 18759, 2022.

[27] Luceda Photonics, "Luceda AWG Designer," 2024. [Online]. Available: https://www.lucedaphotonics.com/luceda-awg-designer

[28] C.-C. Yang and W.-C. Chen, "The structures and properties of hydrogen silsesquioxane (HSQ) films produced by thermal curing," *Journal of Materials Chemistry*, vol. 12, pp. 1138–1141, 2002.

[29] N. Le Thomas, A. Dhakal, A. Raza, F. Peyskens, and R. Baets, "Impact of fundamental thermodynamic fluctuations on light propagating in photonic waveguides made of amorphous materials," *Optica*, vol. 5, no. 4, pp. 328–336, Apr 2018.